J. Fluid Mech. (2010), *vol.* 646, *pp.* 363–373. © Cambridge University Press 2010
doi:10.1017/S0022112009993338

Shock emission from collapsing gas bubbles

S. J. SHAW† AND P. D. M. SPELT‡
Department of Chemical Engineering, Imperial College London SW7 2AZ, UK

(Received 2 June 2009; revised 6 November 2009; accepted 7 November 2009)

The origin and the resultant properties of the strong pulses or shocks emitted by collapsing gas bubbles into a surrounding liquid are investigated numerically. The compressible flow in both phases is resolved. Results are presented for micron- and millimetre-sized bubbles and for bubble collapse triggered either by an acoustic driving or by an initially imposed spherical shock in the liquid. The origin of the diverging shocks is investigated, and the results of a parametric study for the acoustically driven collapse reveal a predominant linear dependence of the shock strength and width on the maximum bubble radius. The results compare favourably with experimental data and agree well with acoustic theory in the limit of weak forcing.

1. Introduction

Freely suspended collapsing bubbles are well known to emit diverging shock waves upon rebounding from minimum volume (Tomita & Shima 1986; Ward & Emmony 1992; Ohl *et al.* 1999; Pecha & Gompf 2000; Lauterborn *et al.* 2001). Predictions of the strength of any emitted shocks are of interest in cavitation and medical applications, for cases where bubbles collapse sufficiently far away from a wall, such that no liquid jets form (typically 2–3 times the maximum bubble radius; cf. Tomita & Shima 1986). Experimentally, initial values are hard to ascertain, as spatial practicalities mean that measurements of any expanding shock are usually taken at a certain distance from the bubble. To address this issue, we simulate the bubble collapse by using numerical techniques, examining not only shock emission but also conditions inside the bubble.

Diverging shock waves have been measured experimentally by several groups (Weninger, Barber & Putterman 1997; Matula *et al.* 1998; Pecha & Gompf 2000; Lauterborn *et al.* 2001; Karng *et al.* 2003). The shock strength for laser-generated bubbles is approximately linearly dependent on the maximum bubble radius (in the mm range), whereas the full width at half maximum (FWHM) levels off at large values of the maximum radius, above 2 mm (Lauterborn *et al.* 2001). The initial velocity of the shock has been measured to be around $4000\,\mathrm{m\,s^{-1}}$ for a 10 μm radius bubble (Pecha & Gompf 2000); Holzfuss, Rüggeberg & Billo (1998) found an averaged value of $2000\,\mathrm{m\,s^{-1}}$ for a 5 μm radius bubble over a distance between 6 and 72 μm from the bubble centre. At later times, the shock velocity approaches an almost constant value of $\sim 1500\,\mathrm{m\,s^{-1}}$. The rate at which the shock strength decays, however, remains unclear, with observations of a decay rate proportional to the inverse of the shock radius (Karng *et al.* 2003) or faster (Pecha & Gompf 2000).

† Present address: Xi'an Jiaotong-Liverpool University, 111 Ren Ai Road, Dushu Lake Higher Education Town, Suzhou, Jiangsu, 215123, China.
‡ Email address for correspondence: p.spelt@imperial.ac.uk

https://doi.org/10.1017/S0022112009993338 Published online by Cambridge University Press

Previous numerical studies of the diverging shock waves radiated by collapsing bubbles have mainly used models where the compressible equations of motion for the liquid are solved by invoking the Kirkwood–Bethe (KB) hypothesis. The motion of the bubble surface is then tracked using a Rayleigh–Plesset-type equation (Gilmore 1952; Hickling & Plesset 1964; Holzfuss *et al.* 1998; Karng *et al.* 2003) that incorporates the effects of the bubble interior, i.e. the equations of motion are not directly simulated within the bubble in conjunction with the KB hypothesis for the liquid flow (with the exception of the work by Karng *et al.* 2003). Though successful in capturing the formation of a diverging shock wave, the resultant predicted shock structure differs from the experimental observation. Karng *et al.* (2003) found the FWHM to be off by a factor of 6. It remains unclear whether this is caused by limitations in the experimental method (Matula *et al.* 1998) or assumptions made in the model.

Here, instead, we solve the directly coupled compressible equations of motion for both phases, negating the need for these assumptions. Most recent two-phase compressible simulations consider the shock-impact-driven breakup of one or two bubbles (e.g. Hu *et al.* 2006). Therein, the accurate simulation of the approach to minimum volume, bubble rebound and the associated shock emission still remains a computational challenge (cf. Nagrath *et al.* 2006; Johnsen & Colonius 2009). An exception is the early work of Moss *et al.* (1994) who, although resolving the compressible flow in the liquid, studied mainly the flow inside spherically collapsing bubbles (albeit employing artificial viscosity to stabilize the numerical method and splitting the simulations into two stages), rather than shock waves radiated by collapsing bubbles.

To address this, we present results of a number of simulations of spherically collapsing bubbles and subsequent shock emission. For millimetre-sized bubbles, this would appear to be a good approximation (cf. Ward & Emmony 1992; Lauterborn *et al.* 2001). For micron-sized bubbles (>5 μm), parametric instability (Holt & Gaitan 1996; Brenner, Hilgenfeldt & Lohse 2002) is important, especially for acoustically driven bubbles, but grows during the expansion phase of the afterbounces and thus spherical symmetry should still be a good approximation during the initial collapse. Rayleigh–Taylor (RT) instability may lead to severe distortion of collapsed vapour bubbles after rebound from minimum volume (Brennen 2002); it is unclear at present whether a diverging shock in water is unstable to non-spherical disturbances, as previous work is primarily on converging shocks in ideal or van der Waals gases (cf. Evans 1996). Even in such cases, however, it is important to have benchmark results for spherically symmetric collapse when attempting three-dimensional simulations (which have the added difficulty that shape modes may result from the discretization used), in order to assess the significance of shape modes on the acoustic emission. If present, we expect a non-strictly spherical collapse to give rise to slightly weaker emissions. We briefly investigate the significance of the RT shape mode instability in § 5.

2. Problem set-up and numerical method

We introduce the spherical symmetric polar coordinate system $\underline{\mathbf{x}} = r\underline{\hat{r}}$ measured with respect to the bubble centre. In each phase, the respective fluids are modelled by the spherically symmetric compressible Euler equations in quasi-conservative form

$$\frac{\partial \boldsymbol{Z}}{\partial t} + \frac{\partial \hat{\boldsymbol{F}}(\boldsymbol{Z})}{\partial r} = S(\boldsymbol{Z}), \quad \boldsymbol{Z} = r^2(\rho, \rho w, E)^{\mathrm{T}}, \quad \hat{\boldsymbol{F}}(\boldsymbol{Z}) = r^2(\rho w, \rho w^2 + p, w[E + p])^{\mathrm{T}}, \tag{2.1}$$

https://doi.org/10.1017/S0022112009993338 Published online by Cambridge University Press

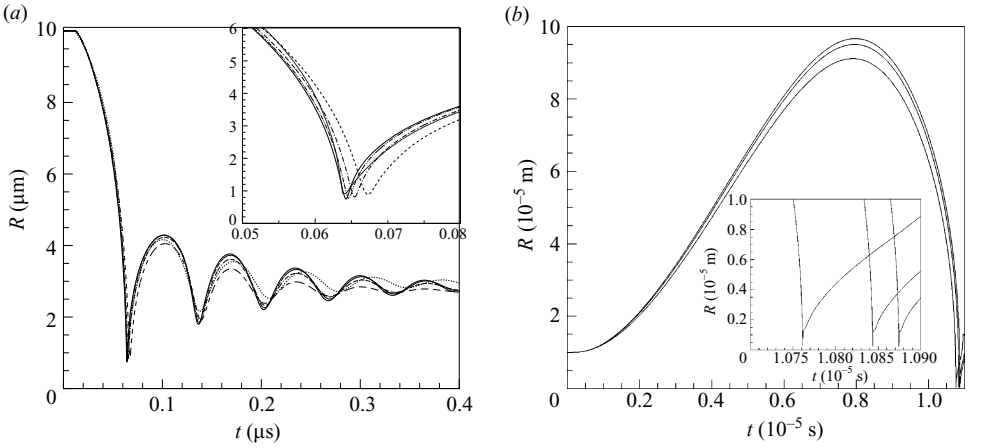


FIGURE 1. Convergence study: bubble radius vs. time (*a*) upon impact of a converging spherical shock wave ($P_0 = 10$ MPa; $R_i = 10\,\mu$m, $R_0 = 3R_i$, $R_1 = 5R_i$), and (*b*) an acoustically driven bubble ($\omega = 5 \times 10^5$ rad s^{-1}, $p_a = 4$ bar, $R_i = 10\,\mu$m, $R_1 = 320\,\mu$m). In (*a*), $N = 1251$ (short-dashed line), 2501 (dash-dotted line), 5001 (dash-dot-dotted line), 10 001 (solid line). The dotted line in (*a*) represents a fit of a Rayleigh–Plesset equation. In (*b*), results are shown (from bottom to top, i.e. from left to right in the inset) for $N =$ 8001, 16 001 and 32 001.

where $S(\mathbf{Z}) = (0, 2rp, 0)^{\mathrm{T}}$, t denotes time, ρ denotes density, p denotes pressure, w denotes the radial velocity and the total energy per unit volume $E = \rho e + 1/2\rho w^2$, e representing the internal energy per unit volume. The effects of viscosity are expected to be small in the strongly forced cases studied here: an upper estimate of the viscous contributions to the pressure in the gas is $\mu_L |\dot{R}|_{max}/R_{min}$, where μ_L denotes the dynamic viscosity of water, R_{min} is the minimum bubble radius and $\dot{R}_{max}$ is the maximum velocity of the bubble surface. For the conditions shown in figure 1(*a*) (which is discussed in detail at the end of this section), $\mu_L = 10^{-3}$ Pa s, $R_{min} \sim 10^{-7}$ m and $|\dot{R}|_{max} \sim 10^3$ m s^{-1}, which would result in a pressure contribution of $O(10^6)$Pa, whereas at minimum volume the pressure is of $O(10^{10})$Pa.

The water surrounding the bubble is modelled by the Tait equation of state, where the ratio of specific heats, $\gamma = 7.15$. For most of the simulations, the ideal gas equation is employed for the bubble interior, where $p = (\gamma - 1)\rho e$. For the acoustic driving case, we have conducted additional simulations using a virial equation of state, $p = \rho \overline{R} T(1 + V_c \rho/(3M)) - 3p_c V_c^2 \rho^2 / M^2$, where T denotes temperature, M denotes molecular mass, $\overline{R}$ denotes specific gas constant, V_c denotes the molar volume at the critical point and p_c denotes the pressure at the critical point, but no significant impact on the results was seen. We have also represented the effects of a constant vapour pressure within the bubble in additional tests, which only caused a smaller decrease in temperature during the expansion stage. The effect of evaporation is further considered at the end of § 3.

In cases where heat conduction is retained, the source term is modified to $S(\mathbf{Z}) = (0, 2rp, (\partial/\partial r)[r^2 \Lambda(\Theta)(\partial\Theta/\partial r)])^{\mathrm{T}}$, where Θ denotes temperature and Λ is the respective fluid's thermal conductivity. Appropriate temperature updates are obtained following Vuong & Szeri (1996).

Equation (2.1) is solved numerically. First, the method of lines is employed to separate the spatial and temporal derivatives. An upwind scheme in characteristic space is used for the spatial fluxes, while the equations are evolved temporally with a third order total variational diminishing Runge–Kutta scheme. The interface is

https://doi.org/10.1017/S0022112009993338 Published online by Cambridge University Press

advected temporally using the appropriately interpolated velocity value. Accurate (and sharp) boundary conditions are imposed at this interface by employing the modified form of the ghost fluid method (Fedkiw 2002) together with the isobaric fix technique (Fedkiw, Marquina & Merriman 1999). A uniform mesh of N grid points is used. Thermal conduction is not accounted for unless stated otherwise; when it is considered, the additional source term is evaluated at each time step using a second-order central difference.

A bubble of initial radius R_i (under room temperature conditions) is forced into collapse by two alternative approaches. In the first approach, the bubble is exposed to an incoming spherical shock wave of strength P_0, which at $t=0$ is located at $r=R_0$. An outflow condition is used as the outer boundary condition in this case. In the second approach, a sinusoidal acoustic forcing is imposed through an inlet condition at the outer boundary of the computation domain (denoted henceforth by $r=R_1$) with a pressure value $p_{atm}-p_a\sin(\omega t)$, where p_{atm} denotes the background ambient pressure, p_a denotes the forcing amplitude and ω denotes the driving (angular) frequency. Therefore, any signal radiated from the bubble that reaches the outer boundary of the computational domain is reflected in the acoustically driven collapse case, but not in the shock-driven collapse. Tests on a computational domain of half the size, for the acoustically driven collapse, reveal no visible difference with figure 4 (the value of R_{max} changed marginally, but the FWHM and shock strength changed accordingly), showing that the present findings are robust. We also note that, if in the acoustically driven collapse case the pressure in a flask is modelled by $p_{amp}\sin(kr/R_f)/r$, where $k\approx 7.725$ (a root of $k-\tan k$), then $p_{amp}=kp_a$. Symmetry conditions are imposed at $r=0$ in all cases.

For the shock-driven collapse, a self-similar solution predicts that the temperature and pressure become singular at the convergence point of the transmitted shock (cf. Brenner *et al.* 2002). Our grid refinement studies without conduction confirm this (and good agreement is found with the self-similar solution): a finer grid results in larger peak values (although this affects only a small region around the bubble centre). Conduction is expected to regularize this behaviour (Vuong & Szeri 1996; Vuong, Szeri & Young 1999). Tests show that although the conditions inside the bubble are affected by conduction, no effect is found here on the emission of the diverging shocks in the liquid, which is the main subject of this paper. For simplicity, we therefore omit conduction in § 3 and provide the test results on the effect of conduction in § 4.

In figure 1, results of a convergence study are presented for the temporal evolution of the bubble radius and an example of each type of induced collapse. Inside the bubble, $\gamma=1.4$. In both cases, the results would indicate convergence upon grid refinement. The results in figure 1(b) have been truncated at the point that the diverging shock, once reflected from $r=R_1$, has reached the bubble surface again, since the resultant bubble dynamics are effected by this reflection. In figure 1(a), it can be seen that the results can be well represented by curve-fitting a solution of the Rayleigh–Plesset equation.

3. Overview of flow behaviour

The emission of diverging waves was found to be qualitatively similar for shock- and acoustically driven collapse. In figure 2, the structure of the emitted pulse or shock is shown for an acoustically driven collapse with $p_{atm}=1$ bar, $\omega=5\times10^5$ rad s^{-1}, $R_i=10\,\mu$m, $R_1=320\,\mu$m, for two values of the driving pressure amplitude p_a. At relatively low values of p_a (less than 1.5 bar), no pulse or shock is emitted (not

https://doi.org/10.1017/S0022112009993338 Published online by Cambridge University Press

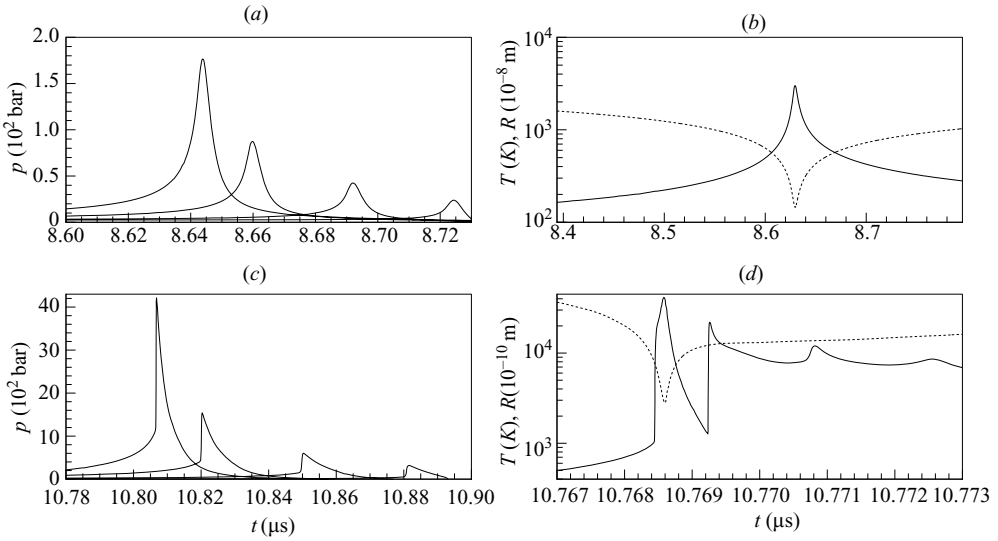


FIGURE 2. Structure of a diverging shock wave (a,c) and the temperature at the bubble centre, together with the bubble radius vs. time (b,d) for an acoustically driven bubble collapse. Driving pressure amplitudes of 1.5 bar (a,b) and 4 bar (c,d), imposed at $r = 160\,\mu$m and for a bubble of initial radius of 10 μm, are used. In (a,c), the pressure is shown at four locations in the liquid, at (from left to right in each panel) $r = 25$, 50, 100 and 150 μm.

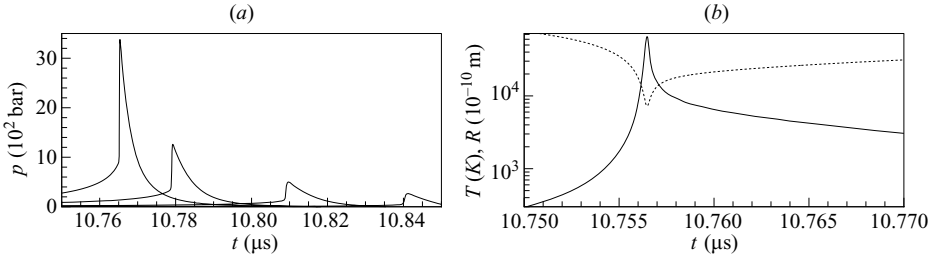


FIGURE 3. Same as in figure 2(c,d) but for $\gamma = 5/3$.

shown). For $p_a = 1.5$ bar (figure 2a), a pulse is emitted, not a shock. It can be inferred from figure 2(b) that the conditions inside the bubble are fairly uniform in this case; the temperature at the bubble centre gradually increases to a peak value at minimum volume and then monotonically decays as the bubble re-expands. For $p_a = 4$ bar (figure 2c), a strong diverging shock wave in the water is observed, as well as the formation of a shock inside the bubble just before minimum volume when conduction is neglected. The extreme temperatures and pressures predicted inside the bubble in this case are unlikely to be observed in experiment and not only because of the effects of conduction. For instance, strongly forced bubbles eventually consist of pure argon (Lohse *et al.* 1997), resulting in a higher value of the ratio of specific heats, γ. In figure 3, we see for the same conditions as in figure 2(c,d), but for $\gamma = 5/3$, no shock is formed inside the bubble, yet a strong diverging shock in the liquid is observed. So, although it seems remarkable that for air–water systems the formation of a clear-cut shock structure (instead of a mere pulse) in the liquid almost coincides with the formation of a shock inside the bubble for the conditions studied here, and neglecting conduction, for noble gas bubbles, a strong diverging shock is observed even if the

https://doi.org/10.1017/S0022112009993338 Published online by Cambridge University Press

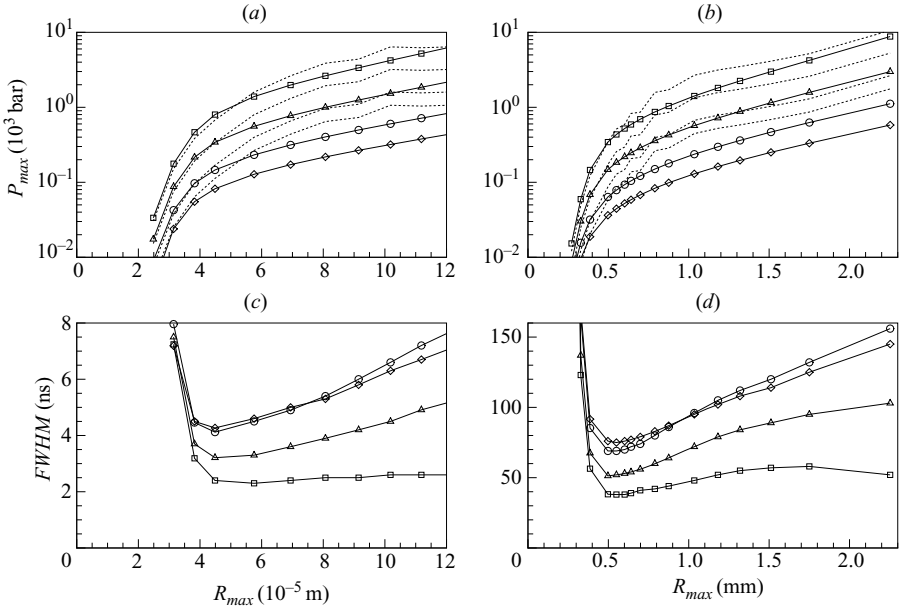


FIGURE 4. The maximum pressure value (a, b) and pulse width FWHM (c, d) in the diverging pulse/shock obtained from different values of p_a for acoustically driven collapse, as a function of the maximum radius of the bubble during the acoustic cycle. In (a) and (c), $R_i = 10\,\mu\text{m}$, $R_1 = 160\,\mu\text{m}$, $\omega = 5 \times 10^5\,\text{s}^{-1}$ and $1.5\,\text{bar} \leqslant p_a \leqslant 5\,\text{bar}$; the symbols are simulation results and the dashed lines represent the corresponding prediction from acoustic theory explained in the main text. In (b) and (d), $R_i = 0.1\,\text{mm}$, $R_1 = 3.2\,\text{mm}$, $\omega = 5 \times 10^4\,\text{s}^{-1}$ and $2\,\text{bar} \leqslant p_a \leqslant 15\,\text{bar}$. Initial conditions are atmospheric. The pressure values were measured at $r = 25$ (□), 50 (Δ), 100 (○) and 150 μm (◇) in (a, c) and at $r = 0.5$ (□), 1(Δ), 2 (○) and 3 mm (◇) in (b, d).

conditions inside the bubble are fairly uniform. We have also verified that the type of regime shown in figure 2(c, d) can be approached for lower driving pressures if the gas has a lower γ value (e.g. by setting $p_a = 2$ bar and $\gamma = 1.1$). The exact sequence of events is further studied in § 4.

The dependency of the pulse/shock peak pressure value and pulse width FWHM for the acoustically driven collapse on the value of the driving pressure amplitude p_a is summarized in figure 4 for relatively small and large bubbles, at different positions in the liquid. In figure 4(a, b), comparisons are also made with the predictions of a simple source in the acoustic limit (Lighthill 1979), $\Delta p = \rho_l \mathrm{d}^2 R^3/\mathrm{d}t^2/(3r)$, where the derivative is evaluated at minimum volume (where $\dot{R} = 0$), giving $\Delta p = \rho_l R^2 \ddot{R}/r$; R and $\ddot{R}$ at minimum volume were obtained by fitting a quadratic function to $R(t)$ around minimum volume, hence the presence of some uncertainty in the theoretical prediction in figure 4. In the vicinity of the bubble, agreement is excellent over the entire range of acoustic forcing studied here, but a substantial overprediction of the emitted shock strength is seen for strong forcing, at large distances from the bubble. From figure 2(c, d) we infer that this stronger decay of the shock waves is accompanied by a broadening in the pulses as they propagate radially outwards (the very rapid change in the FWHM for weak pulses is because of the half-width in these cases being taken at pressure values close to the ambient conditions around the pulse). On a linear scale, for the regimes shown in figure 2(a, d), the dependency on the maximum radius is approximately linear. For stronger forcing (figure 2c, d), there is a departure from this linear relation. The pulse width is seen in figure 4(c) to be only weakly

https://doi.org/10.1017/S0022112009993338 Published online by Cambridge University Press

dependent on R_{max} for sufficiently strong forcing when measured near the collapsing bubble, but to increase approximately linearly for larger values. The results for a larger bubble (figure 4*b*, *d*) are seen to be qualitatively similar, with the exception of the FWHM, which levels off at large R_{max} near the bubble. The minimum value of R_{max} for pulse emission has increased approximately by the same factor as the initial bubble radius (i.e. a factor of ten). Although a quantitative comparison with the corresponding experimental data of Lauterborn *et al.* (2001) is not possible, as those authors studied laser-generated bubbles, it is encouraging to see that the measured shock strength and the FWHM are of the same order as in the experiments. A close inspection of figure 4(*b*) reveals that the pulse strength measured at $r = 3$ mm by an acoustically driven bubble that reaches a maximum radius of $R_{max} = 1$ mm (2 mm) is approximately 130 bar (460 bar). Lauterborn *et al.* (2001) measured at these values of R_{max}, for laser-induced bubbles, values of approximately 80 and 160 bars, respectively. The comparison of the FWHM yields similar results: 95 ns (135 ns) in the simulations versus 65 ns (100 ns). In the experiments, the FWHM shows a linear increase with R_{max} for $0.5\,\text{mm} \leqslant R_{max} \leqslant 2\,\text{mm}$, $45\,\text{ns} \leqslant \text{FWHM} \leqslant 100\,\text{ns}$, and a subsequent saturation, similar to that in the simulations relatively close to the collapsing bubble in figure 4(*d*).

Although evaporation is the subject of our future work, the present method can be used to estimate its effect on the observed properties of emitted shocks presented above, by using a larger initial bubble mass. The simulations of Matula *et al.* (2002), although they do not account for shock emission, suggest a strong increase in the mass of the bubble during the expansion stage of an initial acoustic cycle. This mass increase would appear to subsequently affect only the bubble dynamics from the collapse stage onwards. In particular, larger afterbounces are predicted but no further significant increase in bubble mass is anticipated. A simple representation of this therefore is to use a larger initial bubble mass in the present simulations. This was found to lead to similar results for the temporal evolution of the bubble radius as observed by Matula *et al.* (2002), but with the added benefit of still capturing the emitted shock. The results show that an increase in the initial gas density leads to a gradual reduction in the emitted shock strength (by a factor of 2 upon reaching the density of water) and an increase in the FWHM (similarly by a factor of 2 or 3, depending on the radial location of the measurement).

4. Formation of diverging shocks

Having investigated the overall flow behaviour in the previous section, we focus here on identifying the sequence of events that lead to the formation of diverging shocks. Since in both the acoustically driven and shock-driven collapses the formation is similar, we concentrate on the latter in this section, for ease of computation and to increase the range of cases considered. We consider primarily the collapse of an air bubble in water with $R_i = 10\,\mu\text{m}$, $P_0 = 100$ bar and $R_1 = 50\,\mu\text{m}$. In terms of the results of § 3, this is found to correspond to conditions inside the bubble near minimum volume similar to those in figure 2(*b*), whereas the shock emitted by the bubble is rather sharp as in figure 2(*c*). Thermal conduction is accounted for here unless indicated otherwise; the conductivities in the gas and liquid are $0.025(\Theta/300)^{0.5}$ and 0.6 $\text{W m}^{-1}\ \text{K}^{-1}$, respectively.

The sequence of events is shown in figure 5 and in the supplementary movie in terms of pressure profiles. Figure 5 focuses on a part of the computational domain near the bubble centre. In figure 5(*a*), the initially transmitted shock is seen to be smoothed by

https://doi.org/10.1017/S0022112009993338 Published online by Cambridge University Press

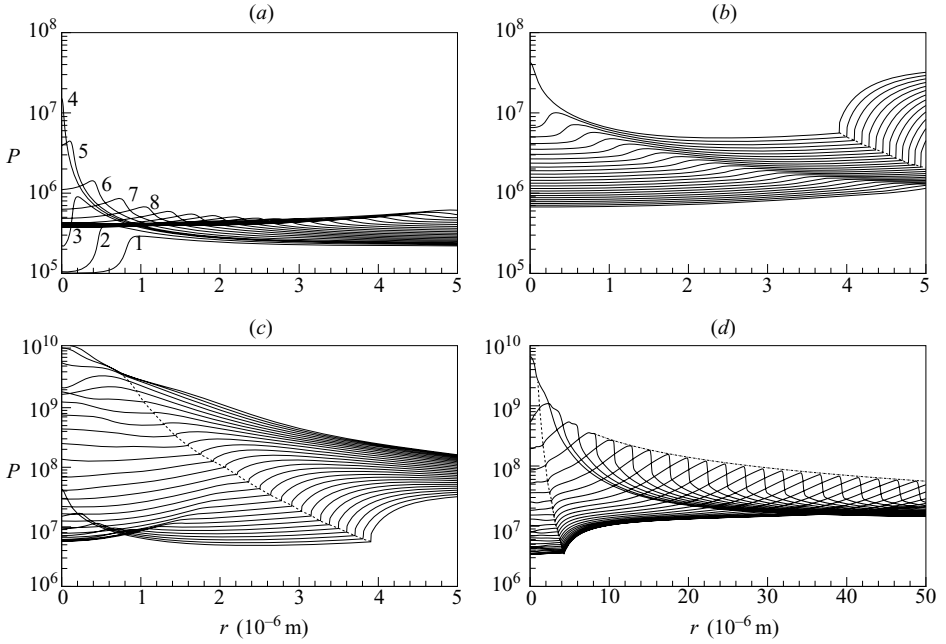


FIGURE 5. Formation of a diverging shock wave for the shock-driven problem (detail) for $P_0 = 100$ bar, $R_i = 10\,\mu$m, $R_1 = 50\,\mu$m, $R_0 = 30\,\mu$m, $N = 10\,001$. (*a–d*) Pressure profiles showing the approach to minimum volume (*a–c*) and the shock formation from nonlinear steepening rather than a reflection from $r = 0$ (*d*). In (*b–d*), the dashed line indicates the bubble radius; the dash-dotted line in (*d*) represents $1/r$.

conduction (the corresponding zero conduction simulation shows a sharp shock at this stage) and to reflect from $r = 0$. Although the resulting reflected shock diverges from the bubble centre through the gas, concurrently the pressure is increasing substantially within the collapsing bubble because of the increased compression, thereby making this reflected shock seem less significant. Subsequent panels were found to be virtually identical with and without conduction. In figure 5(*b*), a pulse has partially reflected from the bubble surface, and this reflection converges back to $r = 0$ where it is reflected from the origin again as can be seen in the final snapshot in figure 5(*b*). (Note, the pressure profiles at subsequent times correspond to those from bottom to the top of the graph.) The collapsing bubble surface is seen to enter the graph on the right at later times. In figure 5(*c*), the newly reflected pulse propagates radially outwards, but seems to play only a minor role in subsequent events. Instead, the dynamics would now appear to be dominated by the continued compression of the bubble contents during the final stages of collapse. Ultimately, the pressure build-up within the bubble is sufficient to reverse the flow initiated by the original shock impact upon the bubble. When this occurs, a large-amplitude pulse/shock is seen to form in figure 5(*d*). Figure 5(*d*) shows the amplitude of the diverging shock decreases approximately as the inverse of the radial coordinate of the shock in this case.

In figure 6(*a*), the radial location of the maximum pressure in the liquid R_m^L is shown together with the bubble radius R versus time. Conduction was found to have no visible effect on these results, except for a minor difference in the conditions at the bubble centre; cf. figure 6(*c*). The effect of the inclusion of heat transfer on the dynamics inside a bubble is further discussed by Lin, Storey & Szeri (2002). At later

https://doi.org/10.1017/S0022112009993338 Published online by Cambridge University Press

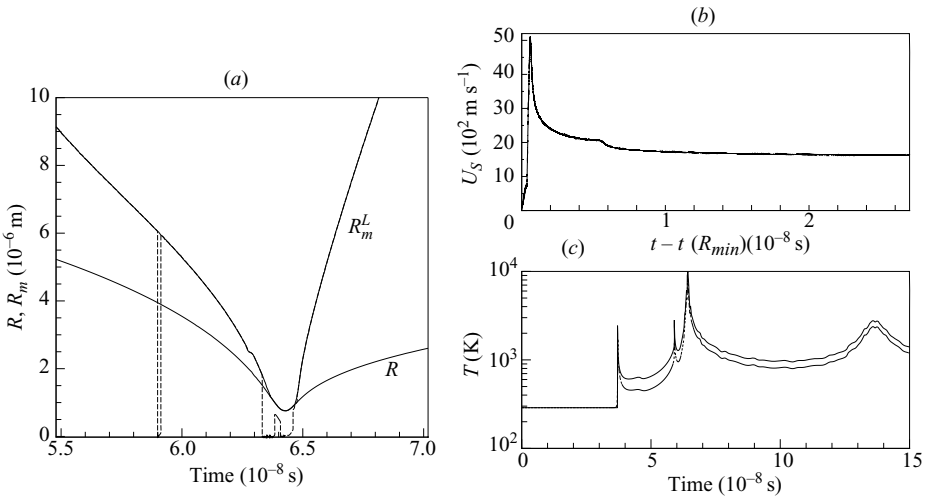


FIGURE 6. For the same simulation as in figure 5. (*a*) Bubble radius and the radial position of the maximum pressure in the liquid vs. time, near minimum bubble volume. The dashed line is the location of the global maximum pressure. (*b*) Velocity of the diverging shock vs. time from minimum volume; (*c*) temperature at the bubble centre as a function of time. In (*c*), both curves are for the same case except that heat conduction is ignored in the upper line. Ignoring conduction resulted in no visible changes to the results shown in (*a*) and (*b*).

times, R_m^L corresponds to the location of the large-amplitude diverging shock in the liquid emitted by the collapsed bubble. This shock location seems to follow naturally from the maximum pressure before minimum volume is reached. Also shown there is the location of the global maximum (the dashed line). After a brief peak at $r = 0$ near $t = 58$ ns, which corresponds to the collapse of the initially transmitted shock (see figure 5*a*), we see that near minimum volume the maximum pressure is in the gas, but not necessarily at $r = 0$. No shocks are observed during this small time period, but the radial location of the maximum pressure is eventually seen to jump towards the bubble surface into the liquid and it is this signal that turns into the diverging shock in the liquid at later times (figure 5*d*).

Finally, we investigate the origin of the shock itself from an emitted pulse. We first note that a close inspection of figure 5(*d*) shows that the emitted pulse is initially double-peaked. This can be seen in the last curve in figure 5(*c*); one peak results from the maximum pressure at $r = 0$, the second to a point in the liquid beyond (behind) which the liquid is moving radially inwards (outwards). In separate numerical work by us, we have found that using the Kirkwood–Bethe hypothesis as summarized by Knapp, Daily & Hammitt (1970) gives a similar initial structure. In this approximate work (not shown here), the double peaks are more pronounced, however, and each develops into separate shocks: one from the meeting of characteristics that originated from the bubble surface before, and one from after, the instance of minimum volume. Subsequently, in figure 5(*d*), it can be seen that these two peaks merge in the full simulations. This leads to an abrupt deceleration of the pressure pulse, as can be seen in figure 6(*b*) at 50 ns after minimum volume. Finally, a shock structure results. The shock speed is seen in figure 6(*b*) to peak at around 5 km s^{-1}, which is similar to values inferred from experiments (see Pecha & Gompf 2000). We have found that this corresponds approximately to the local speed of sound in the liquid (incidentally, the maximum value of the local Mach number based on the instantaneous, local speed

https://doi.org/10.1017/S0022112009993338 Published online by Cambridge University Press

of sound in the liquid during this simulation is around 0.3). Finally, the rate at which the shock speed approaches the sound speed in undisturbed water is rather similar to that measured by Pecha & Gompf (2000) for acoustically driven collapse.

5. Conclusions

Through numerical simulation we show that the strong pressure build-up in the vicinity of the bubble surface during the later stages of bubble collapse develops into a diverging shock (figure 5). The results establish that diverging shocks are not the result of an earlier reflection of a converging shock from the bubble centre. Indeed, for the strong acoustically driven collapse of air bubbles in water, the converging and diverging shocks develop at approximately similar times for the cases studied. The emitted shock strength and width are approximately linear in the maximum radius of acoustically driven bubbles for relatively small and large bubbles. For relatively weak pulses, the shock strength is well predicted by acoustic theory and decays approximately as the inverse radial location of the shock. The strength of relatively strong pulses is generally overpredicted by acoustic theory and decays faster than $1/r$. A comparison of the simulated shock strength and width with Lauterborn *et al.* (2001)'s experimental measurements is encouraging, given that the simulations are for acoustically driven collapse, whereas the experiments are for laser-generated bubbles. The simulated propagation speed of the diverging shock is quite close to that measured by Pecha & Gompf (2000). Initial tests show the potential of mass transfer across the bubble surface to affect these results, and our future work aims to incorporate this.

Finally, this work also provides benchmark data for axisymmetric and three-dimensional two-phase compressible solvers. Shape deformation is the subject of future work; integrating a simplified evolution equation for the leading order shape mode, $\ddot{a}_2 = \ddot{R}a_2/R$ (using $R(t)$ from the simulations), only predicts a five-fold amplification of a_2 from the minimum volume region to the first measurement station of the diverging shock, used for figure 4(b). Consistent with the findings of Prosperetti & Hao (1999) and Brenner *et al.* (2002) for the systems studied in this paper, the RT instability mechanism may not be significant.

Financial support from EPSRC under grants EP/D50371X/1 and EP/046029/1 is acknowledged.

REFERENCES

Brennen, C. E. 2002 Fission of collapsing cavitation bubbles. *J. Fluid Mech.* **472**, 153–166.

Brenner, M. P., Hilgenfeldt, S. & Lohse, D. 2002 Single-bubble sonoluminescence. *Rev. Mod. Phys.* **74**, 425–484.

Evans, A. K. 1996 Instability of converging shock waves and sonoluminescence *Phys. Rev.* E **54**, 5004–5011.

Fedkiw, R. P. 2002 Coupling an Eulerian fluid calculation to a Lagrangian solid calculation with the ghost fluid methods. *J. Comp. Phys.* **175**, 200–224.

Fedkiw, R. P., Marquina, A. & Merriman, B. 1999 An isobaric fix for the overheating problem in multimaterial compressible flows. *J. Comp. Phys.* **148**, 545–578.

Gilmore, F. R. 1952 The growth or collapse of a spherical bubble in a viscous compressible liquid. ONR Rep. No. 26-4.

Hickling, R. & Plesset, M. S. 1964 Collapse and rebound of a spherical bubble in water. *Phys. Fluids* **7**, 7–14.

https://doi.org/10.1017/S0022112009993338 Published online by Cambridge University Press

Holzfuss, J., Rüggeberg, M. & Billo, A. 1998 Shock wave emissions of a sonoluminescing bubble. *Phys. Rev. Lett.* **81**, 5434–5437.

Holt, R. G. & Gaitan, D. F. 1996 Observation of stability boundaries in the parameter space of single bubble sonoluminescence. *Phys. Rev. Lett.* **77**, 3791–3794.

Hu, X. Y., Khoo, B. C., Adams, N. A. & Huang, F. L. 2006 A conservative interface method for compressible flows. *J. Comp. Phys.* **219**, 553–578.

Johnsen, E. & Colonius, T. 2009 Numerical simulations of non-spherical bubble collapse. *J. Fluid Mech.* **629**, 231–262.

Karng, S. W., Lee, Y. P., Kim, K.-Y. & Kwak, H.-Y. 2003 Implosion mechanism for a sonoluminescing gas bubble. *J. Korean Phys. Soc.* **43**, 135–144.

Knapp, R. T., Daily, J. W. & Hammitt, F. G. 1970 *Cavitation.* McGraw-Hill.

Lauterborn, W., Kurz, T., Schenke, C., Lindau, O. & Wolfrum, B. 2001 Laser-induced bubbles in cavitation research. In *IUTAM Symposium on Free Surface Flows* (ed. A. C. King & Y. D. Shikhmurzaev), pp. 169–176. Kluwer.

Lighthill, J. 1979 *Waves in Fluids.* Cambridge University Press.

Lin, H., Storey, B. D. & Szeri, A. J. 2002 Inertially driven inhomogeneities in violently collapsing bubbles: the validity of the Rayleigh–Plesset equation. *J. Fluid Mech.* **452**, 145–162.

Lohse, D., Brenner, M. P., Dupont, T. F., Hilgenfeldt, S. & Johnston, B. 1997 Sonoluminescing air bubbles rectify argon. *Phys. Rev. Lett.* **78**, 1359–1362.

Matula, T. J., Hallaj, I. M., Cleveland, R. O., Crum, L. A., Moss, W. C. & Roy, R. A. 1998 The acoustic emissions from single-bubble sonoluminescence. *J. Acoust. Soc. Am.* **103**, 1377–1382.

Matula, T. J., Hilmo, P. R., Storey, B. D. & Szeri, A. J. 2002 Radial response of individual bubbles subjected to shock wave lithotripsy pulse *in vitro*. *Phys. Fluids* **14**, 913–921.

Moss, W. C., Clarke, D. B., White, J. W. & Young, D. A. 1994 Hydrodynamic simulations of bubble collapse and picosecond sonoluminescence. *Phys. Fluids* **6**, 2979–2985.

Nagrath, S., Jansen, K., Lahey Jr., R. T. & Akhatov, I. 2006 Hydrodynamic simulation of air bubble implosion using a level set approach. *J. Comp. Phys.* **215**, 98–132.

Ohl, C.-D., Kurz, T., Geisler, R., Lindau, O. & Lauterborn, W. 1999 Bubble dynamics, shock waves and sonoluminescence. *Phil. Trans.* A **357**, 269–294.

Pecha, R. & Gompf, B. 2000 Microimplosions: cavitation collapse and shock wave emission on a nanosecond time scale. *Phys. Rev. Lett.* **84**, 1328–1330.

Prosperetti, A. & Hao, Y. 1999 Modelling of spherical gas bubble oscillations and sonoluminescence. *Phil. Trans. R. Soc. Lond.* A **357**, 203–223.

Tomita, Y. & Shima, A. 1986 Mechanisms of impulsive pressure generation and damage pit formation by bubble collapse. *J. Fluid Mech.* **169**, 535–564.

Vuong, V. Q. & Szeri, A. J. 1996 Sonoluminescence and diffusive transport. *Phys. Fluids* **8**, 2354–2364.

Vuong, V. Q., Szeri, A. J. & Young, D. A. 1999 Shock formation within sonoluminescence bubbles. *Phys. Fluids* **11**, 10–17.

Ward, B. & Emmony, D. C. 1992 Interferometric studies of pressures developed in a liquid during infra-red-laser-induced cavitation-bubble oscillation. *Infrared Phys.* **32**, 489–515.

Weninger, K. R., Barber, B. P. & Putterman, S. J. 1997 Pulsed Mie scattering measurements of the collapse of a sonoluminescing bubble. *Phys. Rev. Lett.* **78**, 1799–1802.

https://doi.org/10.1017/S0022112009993338 Published online by Cambridge University Press